Global surface wave diffraction tomography

Michael H. Ritzwoller, Nikolai M. Shapiro, Mikhail P. Barmin, and Anatoli L. Levshin
Center for Imaging the Earth's Interior, Department of Physics, University of Colorado at Boulder, Boulder, Colorado, USA

Received 21 January 2002; revised 16 April 2002; accepted 12 September 2002; published 11 December 2002.

[1] We determine the effect of replacing geometrical ray theory in surface wave tomography with scattering theory. We describe a tomographic method based on a simplified version of the scattering sensitivity kernels that emerge from the Born or Rytov approximations in which surface wave travel times are a weighted average of phase or group slowness over the first Fresnel zone of the wave. We apply this "diffraction tomography" to Rayleigh and Love wave group velocity measurements to produce group velocity maps from 20 to 150 s period on a $2^\circ \times 2^\circ$ grid globally. Using identical data and damping parameters, we also produce maps using "Gaussian tomography" which is based on ray theory with intuitive Gaussian smoothing constraints. Significant differences in the amplitude and geometry of the imaged features appear primarily at long periods but exist even in the short-period maps in regions where average path lengths are large. Diffraction tomography, therefore, is significant in most oceanic regions at all periods, but it is also important on continents at long periods at least. On average, diffraction tomography produces larger velocity anomalies in a period-dependent band of spherical harmonic degrees, and diffraction and Gaussian tomography maps decorrelate past a critical spherical harmonic degree that also depends on period. The widths of resolving kernels that emerge from diffraction tomography are systematically larger than those from Gaussian tomography. Finally, mantle features inferred from diffraction tomography tend to have larger amplitudes and extend deeper than those from Gaussian tomography. *INDEX TERMS:* 7218 Seismology: Lithosphere and upper mantle; 7255 Seismology: Surface waves and free oscillations; 7260 Seismology: Theory and modeling; *KEYWORDS:* surface waves, lithosphere, upper mantle, diffraction, Fresnel zone, tomography

Citation: Ritzwoller, M. H., N. M. Shapiro, M. P. Barmin, and A. L. Levshin, Global surface wave diffraction tomography, *J. Geophys. Res.*, *107*(B12), 2335, doi:10.1029/2002JB001777, 2002.

1. Introduction

[2] Surface wave tomography of both fundamental and overtone modes has undergone explosive growth in recent years. Largely because of its simplicity, geometrical ray theory has played a central role in most of this research and has formed the basis for fundamental advances in our understanding of mantle structure and dynamics. Ray theory, however, tends to break down in the presence of heterogeneities whose length scale is comparable to the wavelength of the wave [e.g., *Woodhouse*, 1974] and is, therefore, considered to be a high frequency approximation. [*Wang and Dahlen*, 1995] clarify the domain of application of ray theory by showing that the width of the first Fresnel zone must be smaller than the scale length of heterogeneity. This places a fundamental limit on the lateral resolution of seismic models based on ray theory. Accurate interpretation of phase and group velocity measurements and the construction of high quality seismic models at length scales less than the average width of the Fresnel zone of the waves must, ultimately, be based on a more accurate model of surface wave propagation than geometrical ray theory provides. Recognition of this fact dates back at least to *Wielandt* [1987].

[3] One way to move beyond the limitations of ray theory is to extend fully coupled free oscillation theory to shorter periods [e.g., *Deuss and Woodhouse*, 2001], but it remains computationally not feasible to apply this in a systematic way at periods below ~100 s. A better method is to use scattering theory for spherical waves. Based on the Born or Rytov approximations, this theory has developed over the past decade and a half in the context of free oscillations [e.g., *Woodhouse and Girnius*, 1982; *Dahlen*, 1987; *Park*, 1987; *Romanowicz*, 1987], surface waves [e.g., *Yomogida and Aki*, 1987; *Snieder and Romanowicz*, 1988; *Friederich*, 1999; *Spetzler et al.*, 2002; *Snieder*, 2002], and body waves [e.g., *Yomogida*, 1992; *Li and Tanimoto*, 1993; *Li and Romanowicz*, 1995; *Marquering and Snieder*, 1995; *Marquering et al.*, 1998; *Pollitz*, 1998; *Marquering et al.*, 1999; *Dahlen et al.*, 2000; *Zhao et al.*, 2000]. These studies differ in the details of the treatments of mode couplings and conversions, forward/backward scattering, single versus multiple scattering [e.g., *Bostock and Kennett*, 1992; *Friederich et al.*, 1993], and whether source directivity is modeled [e.g., *Meier et al.*, 1997]. To date, the use of scattering theories in the estimation of dispersion maps or Earth models has been fairly rare [e.g., *Yomogida and Aki*, 1987; *Li and Romano-*

0148-0227/02/2002JB001777$09.00

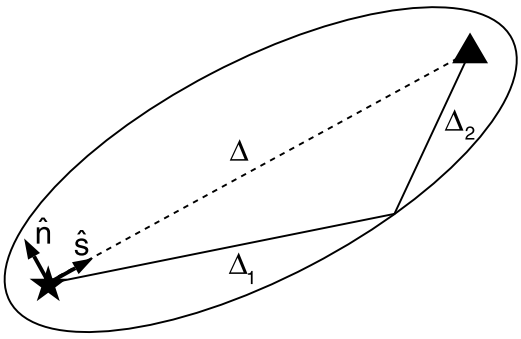

Figure 1. The first Fresnel zone is an ellipse on a sphere with the source (star) and receiver (triangle) at the two foci.

wicz, 1996; *Katzman et al.*, 1998] but is becoming increasingly common [e.g., *Friederich*, 2001; *Yoshizawa and Kennett*, 2001; *Zhao et al.*, 2001; *Spetzler et al.*, 2002].

[4] The common purpose of the advancements in the scattering theories is to model the effects of the finite zone of sensitivity of a traveling wave and the fact that travel time anomalies are not conserved during the propagation of the wave, a phenomenon known as wave front healing [e.g., *Wielandt*, 1987; *Nolet and Dahlen*, 2000]. These advances are applicable to surface waves as well as body waves. The application is actually much simpler for fundamental mode surface waves whose structural sensitivities collapse into two dimensions. In addition, mode couplings, which are important to concentrate the sensitivity kernels near the body wave "ray", are much less important for surface waves. (The exception may be Rayleigh-Love fundamental mode coupling in source regions, as discussed by [*Meier et al.*, 1997].) The scattering theories based on the Born or Rytov approximations typically reduce to performing integrals over a finite area or volume to estimate travel time or phase perturbations caused by structural heterogeneities. Estimation of surface wave sensitivity kernels dates back to [*Woodhouse and Girnius*, 1982].

[5] In this paper we apply a particularly simple form of surface wave scattering theory to broadband group velocity tomography on a global scale and document the principal effects on the estimated tomographic maps and resulting shear velocity model. As discussed in section 2, the theory that we apply is founded on surface wave scattering or Fréchet kernels that are simplifications of the Born/Rytov kernels. We ignore mode couplings, multiple scattering, and source directivity effects. Other simplifications include using Fréchet kernels computed with a 1-D model (PREM) to eliminate the detailed ray tracing needed to identify the first Fresnel zone through a more realistic model (e.g., Fresnel area ray tracing of *Yoshizawa and Kennett* [2002]), and using phase velocity kernels for the group velocity kernels. *Nolet and Dahlen* [2000] and *Spetzler et al.* [2002] discuss differences between the group and phase kernels.

[6] In previous work we performed surface wave tomography based on geometrical ray theory and largely ad hoc Gaussian smoothing constraints [e.g., *Barmin et al.*, 2001; *Levshin et al.*, 2001; *Ritzwoller et al.*, 2001], which we call here "Gaussian tomography." In contrast, we refer to the surface wave tomography based on the simplified form of the Born/Rytov scattering theory as "diffraction tomography." Our motivation is purely practical. We aim to improve global models of the lithosphere and asthenosphere derived from surface wave dispersion information by applying a theory that renders measurements made on short and long paths more consistent and which provides physically based smoothing criteria to the estimated maps. Because of numerous simplifications and approximations, the scattering theory that we apply here probably is at an early stage in the evolution of scattering theories in regional and global tomography. We argue, however, that it represents a significant improvement over geometrical ray theory with purely ad hoc smoothing constraints.

[7] In section 2, we discuss the particular form of scattering theory applied in this paper. The data used in the tomographic inversions are discussed in section 3, and we show how the geometrical ray theoretic travel times of fundamental mode surface waves differ from those computed with scattering sensitivity kernels. The results of diffraction tomography and Gaussian tomography are compared in section 4, and we discuss resolution in section 5. All results are for a data set that extends across the globe, and the group velocity tomography is performed globally, so comparisons are global averages. Regional variations from the statistics we present exist but are not discussed in this paper in detail.

2. Fresnel Zones and Sensitivity Kernels

[8] The region over which surface waves scatter is defined by an ellipse on a sphere given by

$$|\Delta - (\Delta_1 + \Delta_2)| = \lambda/N, \tag{1}$$

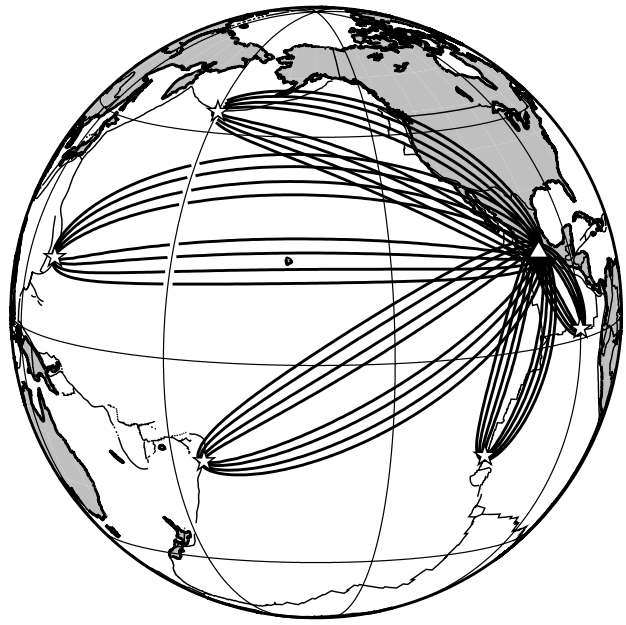

Figure 2. Rayleigh wave sensitivity zones (N = 8/3) for waves observed in Mexico (triangle) originating from several epicentral regions (stars): Galapagos (2087 km), East Pacific Rise (4493 km), Aleutians (7777 km), Tonga (8916 km), and the Marianas (11700 km). These sensitivity zones are for 20 s, 50 s, 100 s, and 150 s Rayleigh waves, where the zone is narrowest at shortest period.

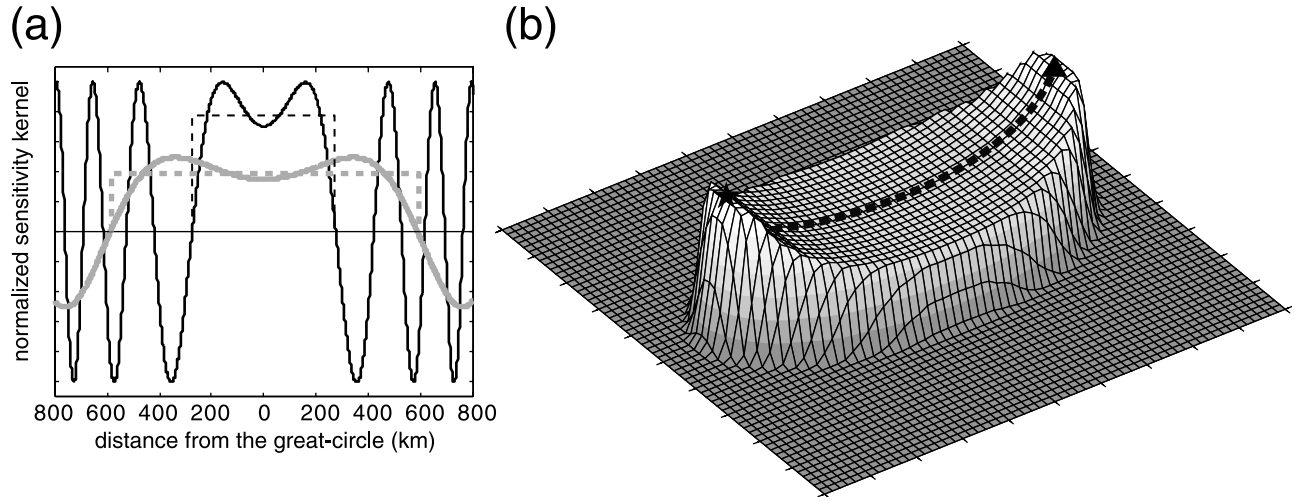

Figure 3. (a) Amplitude of the scattering Fréchet kernel transverse to the source-receiver path at the path midpoint for the 50 s Rayleigh wave. Solid lines are the Born/Rytov approximation kernels [*Spetzler et al.*, 2002] for epicentral distances of 2000 km and 8000 km, respectively, and dashed lines are the approximation we use here in diffraction tomography. (b) Idealized example of the full Fréchet kernel used in diffraction tomography, illustrating how the amplitude of sensitivity increases near source (star) and receiver (triangle).

as shown in Figure 1, where λ is the wavelength of the wave of interest determined from PREM [*Dziewonski and Anderson*, 1981]. The first Fresnel zone encompasses all scatterers whose combined distance from the source and receiver is less than half a wavelength greater than the source-receiver geodetic distance. This corresponds to all signals that will arrive within half a period of the first arrival, and in this case, $N = 2$.

[9] The optimal value of N to model the scattering sensitivity of surface waves on a sphere remains the subject of debate. [*Yoshizawa and Kennett*, 2002] argue that the primary "zone of influence" spans only about one-third of the width of the first Fresnel zone, so $N = 18$ is the value that should be used in surface wave tomography. [*Spetzler et al.*, 2002] argue that $N = 8/3$ is the value that is consistent with the Born/Rytov approximation. To retain consistency with the Born/Rytov approximation, we will use $N = 8/3$ here. We will refer to the region so defined as the "sensitivity zone," which is a subset of the first Fresnel zone. Sensitivity zone widths, irrespective of the choice of N,

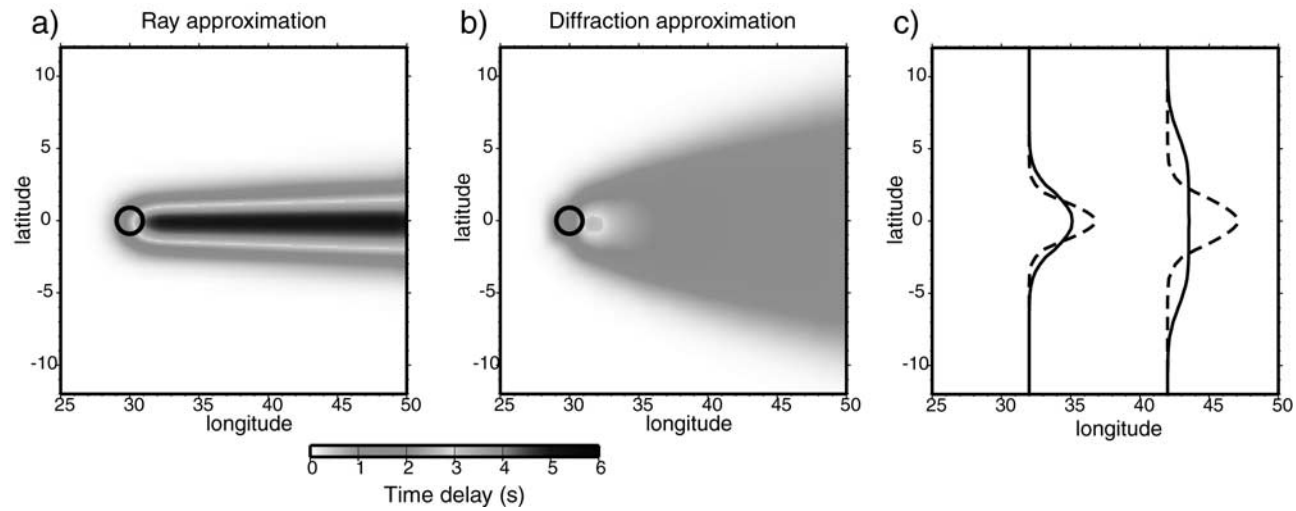

Figure 4. The effect of a small scatterer in the (a) ray theoretic and (b) diffraction approximations. The scatterer is circular, with a Gaussian-shaped cross section with $\sigma = 1°$ located 30° (3333 km) from the source. In the ray approximation, the scatterer casts a narrow travel time shadow whose amplitude and width change minimally with distance from the scatterer. In the diffraction approximation the shadow widens and the amplitude decays to model wave front healing. (c) Profiles across the travel time shadow at 32° and 43° from the source (2° and 13° from the scatterer). The diffraction shadow is flat due to the "boxcar" shape of the scattering sensitivity kernel transverse to the wave path (Figure 3b). Diffraction lowers the amplitude of a travel time perturbation relative to ray theory.

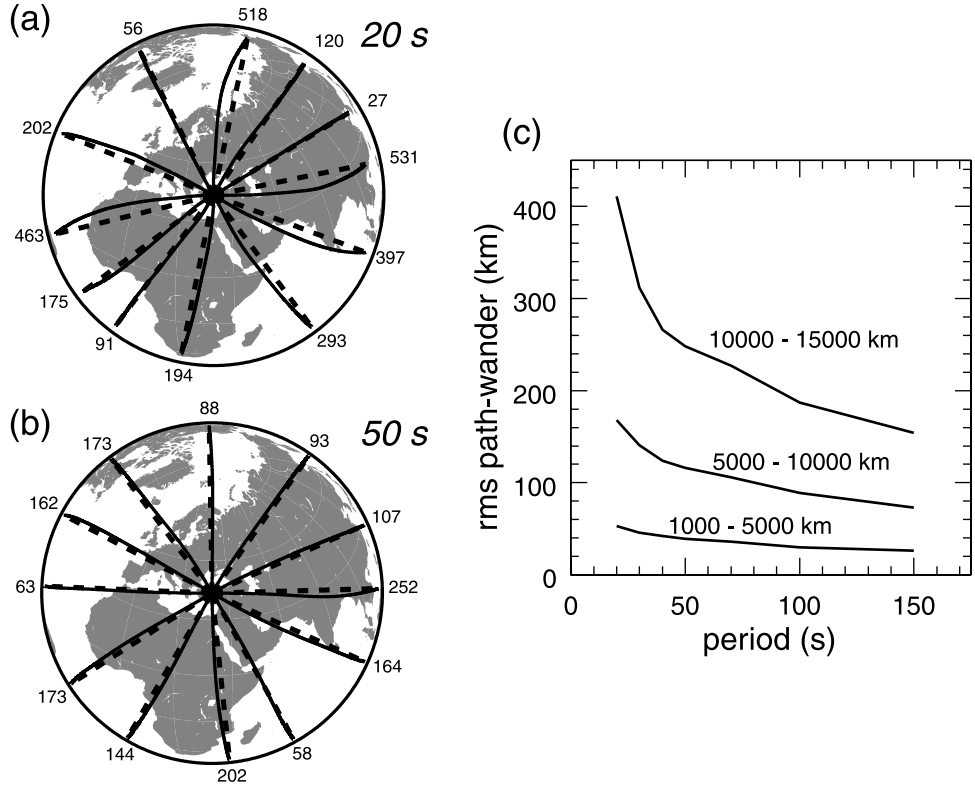

Figure 5. Path wander of geometrical rays. (a) Minimum travel time rays (solid lines) computed through the model of *Shapiro and Ritzwoller* [2002] for the 20 s Rayleigh wave compared with the great circle (dashed lines) from source to receiver. Rays emanate from a source in Turkey and travel 70°. Maximum path wander in kilometers is indicated outside the globe for each path. (b) Same as Figure 5a, but for the 50 s Rayleigh wave. (c) RMS of path wander as a function of period, segregated by path length, for the data set described in section 3.

grow with period and path length, as illustrated by Figure 2. The details of our results will depend on the value of N chosen to define the extent of the surface wave sensitivity zone. As N grows, the distinction between ray and scattering theories blurs. Our primary conclusions are relatively robust with respect to this choice, however. The definition of the sensitivity zone given by equation (1) is based on the 1-D model PREM. This is a reasonable starting point, but can be refined by tracing rays through phase velocity maps derived from a 3-D model, as done by [*Yoshizawa and Kennett*, 2002].

[10] Inspired by the Born/Rytov approximation, we determine surface wave travel times by performing an area integral over the surface of the Earth:

$$t_q^{\mathrm{diff}}(\omega) = \int_0^{2\pi} \int_0^{\pi} K_q(s,n,\omega) v_q^{-1}(s,n,\omega) \sin(s) ds dn, \qquad (2)$$

where K_q is suitably normalized on an ellipsoidal Earth to give v_q the units of m/s. Without loss of generality, we consider the source at the pole so that the epicentral coordinates n and s are identified with longitude and colatitude, respectively, as in Figure 1. The expression $K_q(s, n, \omega)$ is the Fréchet or scattering sensitivity kernel which depends on wave type q (Rayleigh, Love) and frequency ω, and v_q is the Rayleigh or Love wave group or phase speed. We will ignore the fact that the kernel will differ somewhat for phase and group velocity, because these differences within the sensitivity zone are probably smaller than other uncertainties in the definition of the Fréchet kernels (e.g., N, the amplitude variation of the kernel). Equation (2) is to be contrasted with the geometrical ray theory travel time:

$$t_q^{\mathrm{rt}}(\omega) = \int_p v_q^{-1}(s,\omega) ds, \qquad (3)$$

which is simply a line integral along the geometrical ray path p.

[11] Fréchet kernels determined from the Born/Rytov approximation oscillate both along and transverse to the source-receiver geodesic. Transverse oscillations are shown in Figure 3a. By a stationary phase argument, the contributions to the travel time that arise outside the central lobe of the Born/Rytov kernel are of higher order than those that result from the central lobe. We approximate the Born/Rytov kernel with a boxcar transverse to the source-receiver geodesic. We, therefore, do not model the central minimum in the Born/Rytov kernel, but neglecting this feature will have a minimal effect on surface wave travel times (although it would have a bigger effect on body waves). Similar to *Vasco et al.* [1995], we scale the amplitude of the Fréchet kernel inversely with the transverse width of the sensitivity zone, as illustrated by Figure 3b. This choice is based purely on the qualitative physical argument that sensitivity to scatterers must maximize where the wave

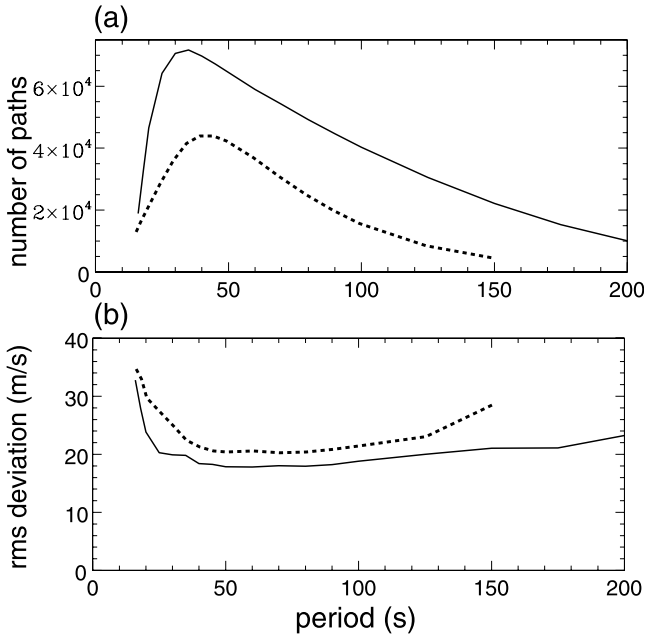

Figure 6. (a) Number of group velocity measurements used in the tomography. (b) RMS deviation among the group velocity measurements within summary rays averaged over all summary rays. This is the estimate of standard data errors. Solid lines, Rayleigh waves; dashed lines, Love waves.

field is most compressed, which is near the source and receiver. The integration in equation (2) extends over the whole Earth but really is confined to the sensitivity zone because outside this zone the Fréchet kernel is zero. Further refinement of the amplitude of the Fréchet kernel between source and receiver is a direction for future research.

[12] With the definition of the Fréchet kernels described here, equation (2) will model waveform healing, as shown in Figure 4. The accuracy of this approach must be verified with numerical experiments in the future but will be about as accurate as the Born/Rytov approximation which it approximates.

[13] Our definition of the Fréchet kernels, which is based on a 1-D model, does not account for the deformation of the sensitivity zone caused by structural heterogeneities. Accounting for this deformation would render the inverse problem nonlinear and is beyond the scope of the present paper. It will be important, however, if the extent of the deformation is a substantial fraction of the width of the sensitivity zone. This is most likely when the sensitivity zone is narrow; i.e., at short periods or if $N \gg 2$ as argued by *Yoshizawa and Kennett* [2002]. The deformation of the sensitivity zone is the scattering analog of path bending of geometrical rays in an inhomogeneous medium. We attempt to quantify the importance of this deformation by investigating geometrical ray bending. To do so, we trace geometrical surface rays through phase velocity maps computed from the shear velocity model of *Shapiro and Ritzwoller* [2002] and compare them to great circular rays for the source-receiver paths in the data set described in section 3. We refer to the maximum deviation between the bent geometrical ray and the great circle as the "path wander" for a source:receiver pair. Examples of bent geometrical rays are shown in Figures 5a and 5b. Figure 5c summarizes the RMS of the path wander over our entire data set. The expected path wander is typically below the estimated resolution (section 5), except for long paths at short periods. At global scales, we believe that this effect can be safely ignored at periods above about 30 s in the context of diffraction tomography, but between periods of 15 and 30 s it may be as important as modeling scattering in regions with strong lateral gradients. It is, nevertheless, ignored here, but deserves concentrated effort in the future.

3. Dispersion Curves: Observations and Predictions

[14] *Ritzwoller and Levshin* [1998] describe in detail the procedure for measuring group velocities. At present, the data set consists of about 130,000 paths globally. Each dispersion curve has been subjected to analyst review to separate the signal of interest from noise and to choose the frequency band of each particular measurement. The number of measurements, therefore, varies as a function of frequency and wave type, as Figure 6a shows. We cluster the measurements into what are commonly called "summary rays" by dividing the Earth's surface into overlapping circular regions of 111 km radius. We look for path endpoints in each pair of circular regions on the globe and cluster all measurements that begin and end in the same pair of regions to produce a summary ray. We average the measurements within each summary ray cluster and reject outliers. Prior to outlier rejection, the RMS deviation of the clustered measurements is taken as the standard error of the summary ray. The RMS of all of these standard errors is

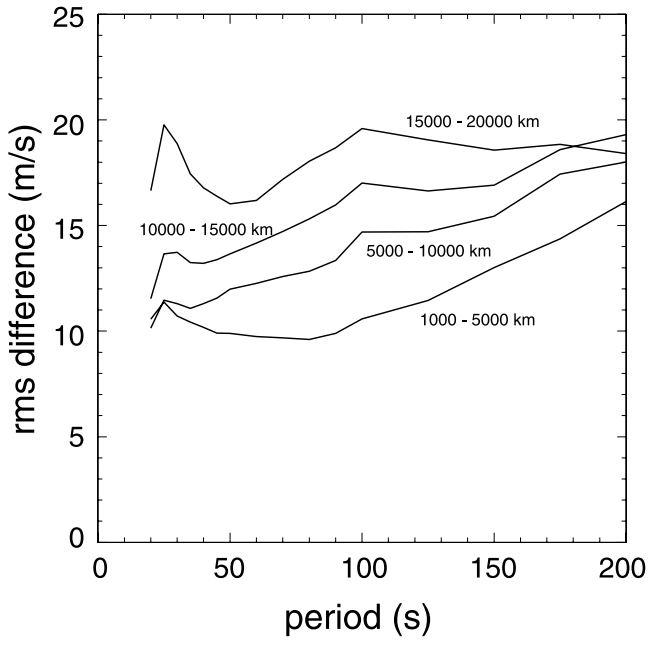

Figure 7. RMS difference between the Rayleigh wave group travel times predicted with ray theory (equation (3)) and diffraction theory (equation (2)) for the source:station paths in the data set described in section 3. Travel times are computed through the diffraction tomography maps, and results are segregated by the path lengths indicated.

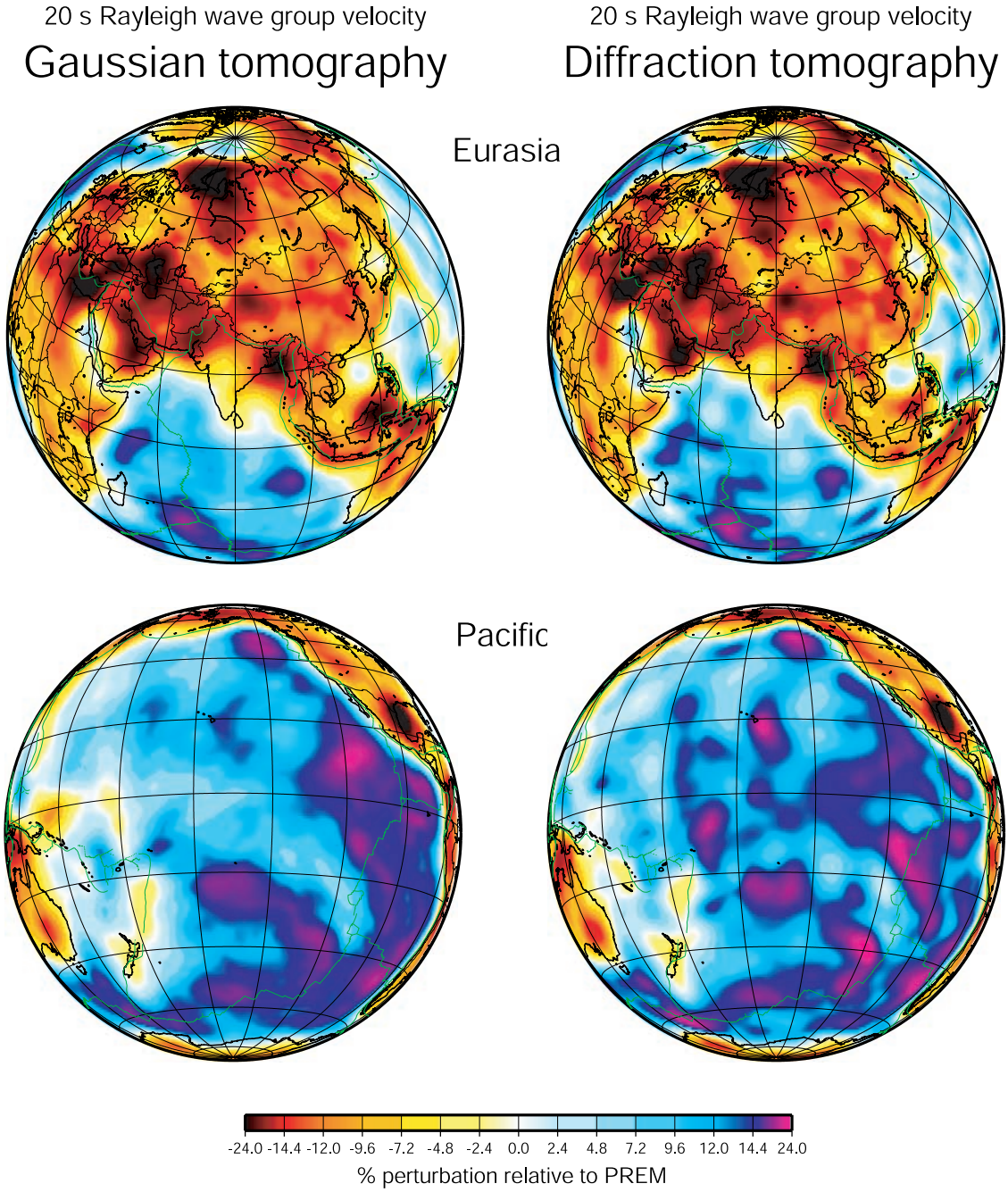

Figure 8. Comparison of the result of Gaussian (ray theory and ad hoc smoothing) and diffraction (fresnel sensitivity kernels and the same ad hoc smoothing) tomography for the 20 s Rayleigh wave group velocity. Results are presented as percent perturbation relative to the group velocity from PREM.

shown in Figure 6b, which we interpret as the average standard error of the measurements. The standard errors for group velocities average about 20 m/s but are somewhat higher at the ends of the frequency band considered.

[15] To quantify the effect of diffraction on surface wave group travel times, we compare predicted travel times computed using equations (2) and (3) applied to the diffraction tomography maps discussed in section 4. Figure 7 presents these results, segregated by path length. Discrepancies from 10 to 20 m/s are common, and typically grow with period and as path length increases, as expected. Differences between ray and diffraction theoretic travel times are important even at periods as low as 20 s because the amplitude of anomalies on the tomographic maps is largest for the short periods. The ray and scattering theory travel times will not converge perfectly even for very short periods because of the finite discretization of the Fréchet kernels (~55 km).

4. Diffraction Tomography

[16] We apply the tomographic method of *Barmin et al.* [2001] to the data set described in section 3 to construct group velocity maps on a $2^\circ \times 2^\circ$ grid world-wide. This method is based on minimizing the following objective

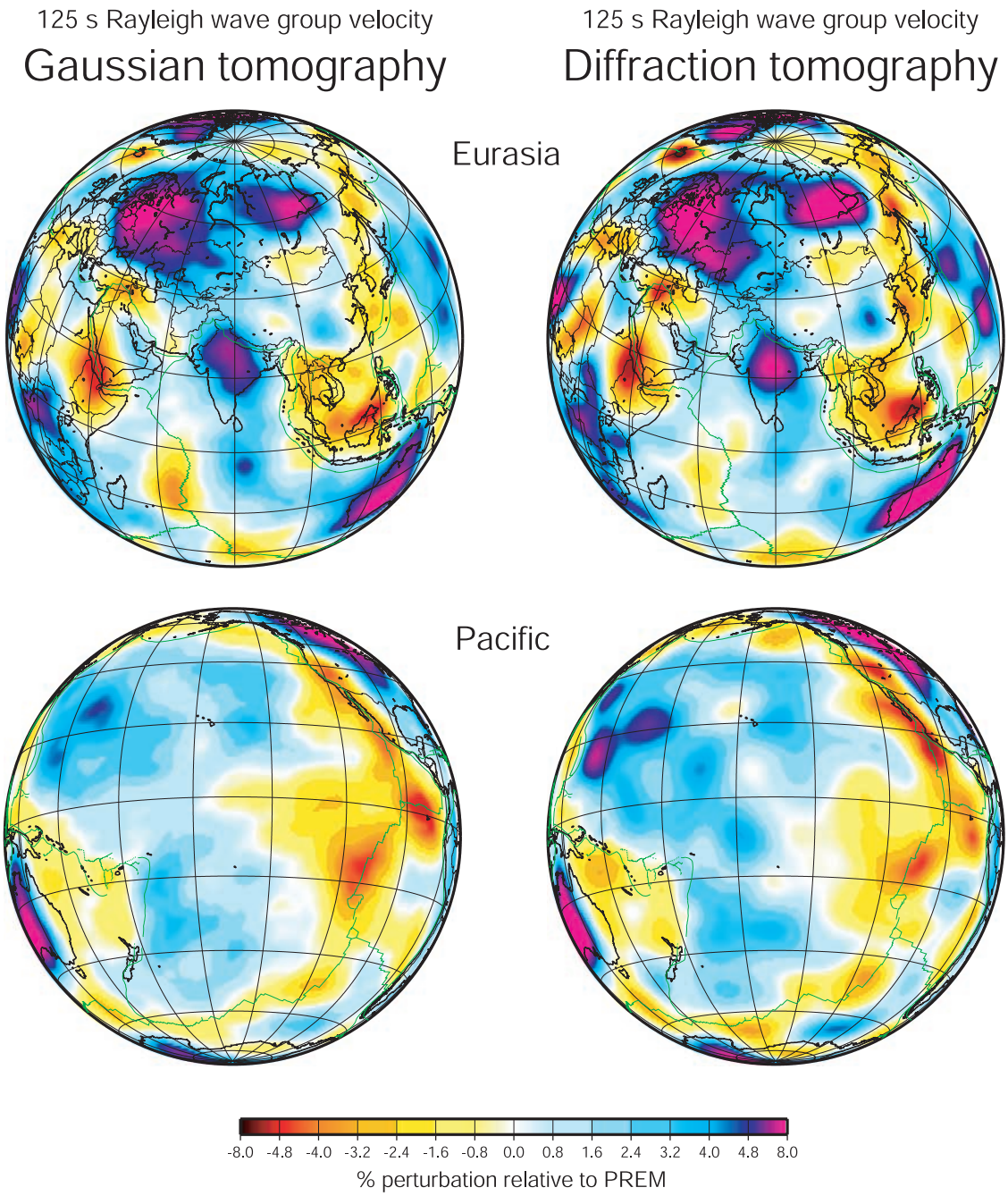

Figure 9. Same as Figure 8, but for the 125 s Rayleigh wave.

function for an isotropic map **m** consisting of velocity perturbations relative to a reference map:

$$(\mathbf{Gm}-\mathbf{d})^T\mathbf{C}^{-1}(\mathbf{Gm}-\mathbf{d})+\alpha^2\parallel F(\mathbf{m})\parallel^2+\beta^2\parallel H(\mathbf{m})\parallel^2 . \quad (4)$$

Equation (4) is a linear combination of data misfit, model roughness, and the amplitude of the perturbation to the reference map. **G** is the forward operator that computes travel time from a map, **d** is the data vector whose components are the observed travel time residuals relative to the reference map, **C** is the data covariance matrix or matrix of data weights, F is a Gaussian spatial smoothing operator, and H is an operator that penalizes the norm of the model in regions of poor path coverage. The method is described in detail by *Barmin et al.* [2001]. We note here that the spatial smoothing operator is defined over a 2-D tomographic map as follows:

$$F(\mathbf{m})=\mathbf{m}(\mathbf{r})-\int_S S(\mathbf{r},\mathbf{r}')\mathbf{m}(\mathbf{r}')d\mathbf{r}', \quad (5)$$

where S is a smoothing kernel:

$$S(\mathbf{r},\mathbf{r}')=K_0\exp\left(-\frac{|\mathbf{r}-\mathbf{r}'|^2}{2\sigma^2}\right), \quad (6)$$

$$\int_S S(\mathbf{r},\mathbf{r}')d\mathbf{r}'=1, \quad (7)$$

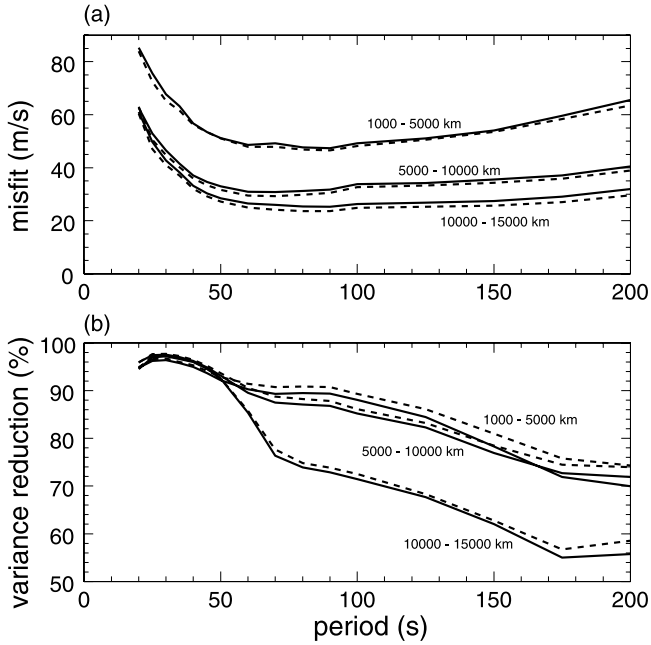

Figure 10. (a) RMS misfit provided by the Rayleigh wave maps to the group velocity measurements. Solid line is diffraction tomography, dotted line is Gaussian tomography. The three lines are for path lengths of 1000–5000 km, 5000–10,000 km, and 10,000–15,000 km. (b) Similar to Figure 10a, but this is variance reduction relative to PREM presented in percent.

and σ is the spatial smoothing width or correlation length. The vector **r** is a position vector on the Earth's surface [**r** = (s, n)]. Values at spatial points between nodes are computed with bilinear interpolation. The choice of the damping coefficients α and β and the smoothing width σ is ad hoc. We typically apply spatial smoothing widths from 150 to 300 km. The difference between ray theoretic and diffraction tomography lies solely in the forward operator **G**. Diffraction tomography uses equation (2), and ray theoretic tomography uses equation (3) in **G**.

[17] The roughness of the ray theoretic dispersion map is completely controlled by the operator F. The Gaussian smoothing operator in equation (4) is similar to using "fat rays" with a Gaussian cross section. For this reason we refer to the ray theory tomography as "Gaussian tomography", because it is, in fact, similar to using Gaussian beams. Some researchers do not consider this, strictly speaking, to be ray theory. In previous applications of this formalism [e.g., *Barmin et al.*, 2001; *Levshin et al.*, 2001; *Ritzwoller et al.*, 2001], we increased σ systematically with period to mimic the widening of sensitivity zones with period. This is similar in spirit to the smoothing operations applied by *Yanovskaya and Ditmar* [1990] and *Lomax* [1994] but is ineffective at modeling how sensitivity zones change shape with path length and, therefore, does not model waveform healing.

[18] The smoothness of the maps estimated with diffraction tomography is not entirely controlled by the smoothing operator F because the finite extent of the sensitivity zone

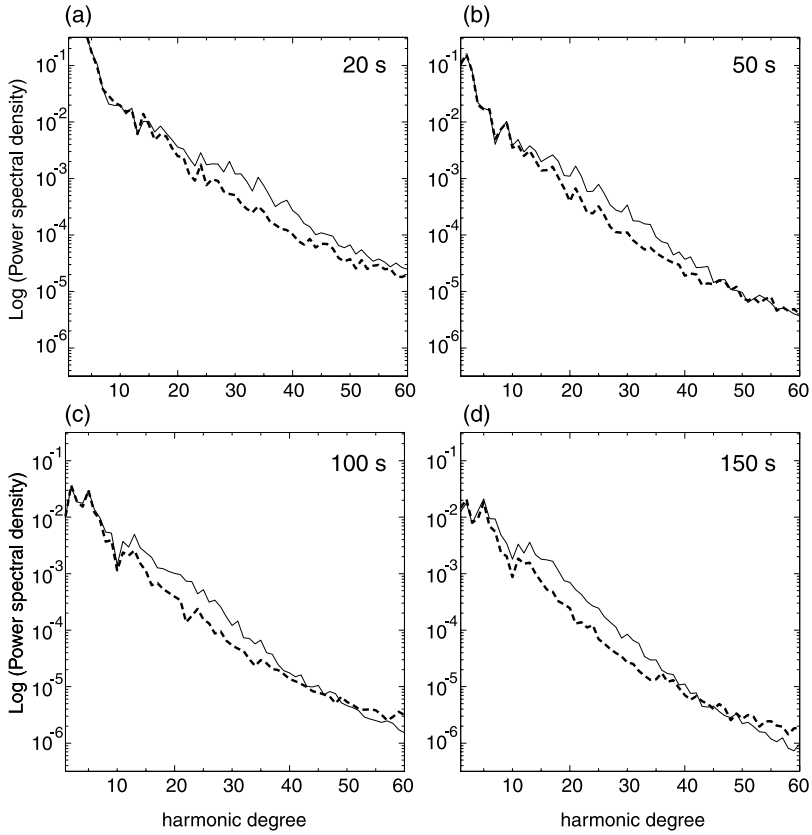

Figure 11. Power spectral density at four periods for the Rayleigh wave group velocity maps constructed by diffraction (solid lines) and Gaussian (dashed lines) tomography, plotted versus spherical harmonic degree (ℓ).

naturally smooths the maps when sensitivity zones are wider than 2σ, which they commonly are except at very short periods or for very short paths. In diffraction tomography the smoothness constraint tends to control the amplitude of the model more than its smoothness. The smoothness of the diffraction tomography maps is more strongly affected by the width of the sensitivity zone.

[19] Examples of Gaussian (i.e., ray theoretic) and diffraction tomography dispersion maps at 20 and 125 s period can be found in Figures 8 and 9. These maps are constructed with identical data and damping parameters. The data are fit about as well with diffraction tomography as Gaussian tomography, as Figure 10 shows. Raw RMS misfits typically lie between 25 and 35 m/s but increase appreciably at the ends of the frequency band and for the shortest wave paths. RMS misfits rise at short periods and for short wave paths because the signal amplitudes increase, but misfits increase at long periods due to degradations in the quality of the travel time measurements. Variance reductions range from ~55% to 98% depending on the period and path length and, in contrast with RMS misfit, are largest where the signal is largest, i.e., at short periods for short paths. This is good, concern over misfit is partially alleviated by the fact that maximum improvement in data fit occurs where there is the maximum misfit.

[20] Diffraction tomography differs most from Gaussian tomography where the first Fresnel zones (or sensitivity zones) are widest. This is typically at long periods and for long paths away from sources and receivers. (Near sources and receivers Fresnel zones taper to $\lambda/4$ in width.) Thus, in regions of good source and/or receiver coverage, Gaussian tomography produces higher fidelity images than in regions well separated from seismogenic zones or receivers. To first-order this means that Gaussian tomography does better in continents than in oceans, as the comparisons centered on Eurasia and the Pacific reveal in Figures 8 and 9. Significant differences between Gaussian and diffraction tomography extend all the way down to 20 s period in the Pacific. This may be surprising, but Figure 2 shows that sensitivity zones for 20 s waves crossing much of the Pacific basin are quite wide. In general, the features in the diffraction tomography maps tend to be somewhat larger spatially, with smoother edges and higher amplitudes than the analogous features in the Gaussian tomography maps. In some regions of the world, however, the pattern of the anomalies is changed at long periods by the use of diffraction tomography.

[21] A more detailed comparison of the Gaussian and diffraction tomography maps is aided by decomposing the maps into spherical harmonics to compare power spectra and cross correlate the maps:

$$m(\theta,\phi) = \sum_{\ell=0}^{\ell_{\max}} \sum_{m=-\ell}^{\ell} c_\ell^m Y_\ell^m(\theta,\phi). \tag{8}$$

We use fully normalized, complex spherical harmonics $Y_\ell^m(\theta, \phi)$ [*Edmonds*, 1960]:

$$\int_0^{2\pi} \int_0^{\pi} Y_\ell^m(\theta,\phi) Y_{\ell'}^{m'*}(\theta,\phi) \sin\theta d\theta d\phi = \delta_{\ell\ell'}\delta_{mm'}, \tag{9}$$

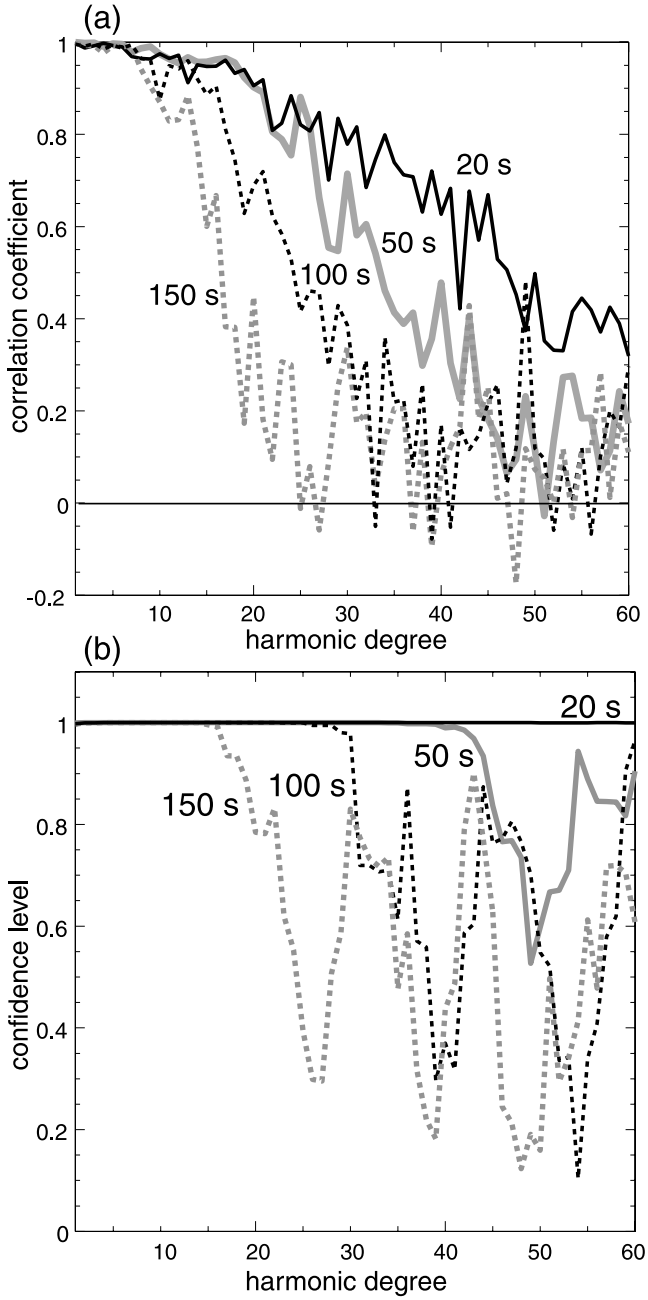

Figure 12. Correlation between the Rayleigh wave group velocity maps constructed by diffraction and Gaussian tomography, plotted versus spherical harmonic degree (ℓ) for four periods. (a) Correlation coefficient. (b) Confidence level of correlation. Because confidence is sensitive to small variations in correlation, it is smoothed by averaging over five adjacent ℓ values.

where the asterisk denotes complex conjugation. To agree with the conventions of other studies of the power spectra of dispersion maps [e.g., *Chevrot et al.*, 1998], we define the power spectral density per unit surface area at spherical harmonic degree ℓ as

$$P(\ell) = \frac{4\pi}{2\ell+1} \sum_{m=-\ell}^{\ell} |c_\ell^m|^2. \tag{10}$$

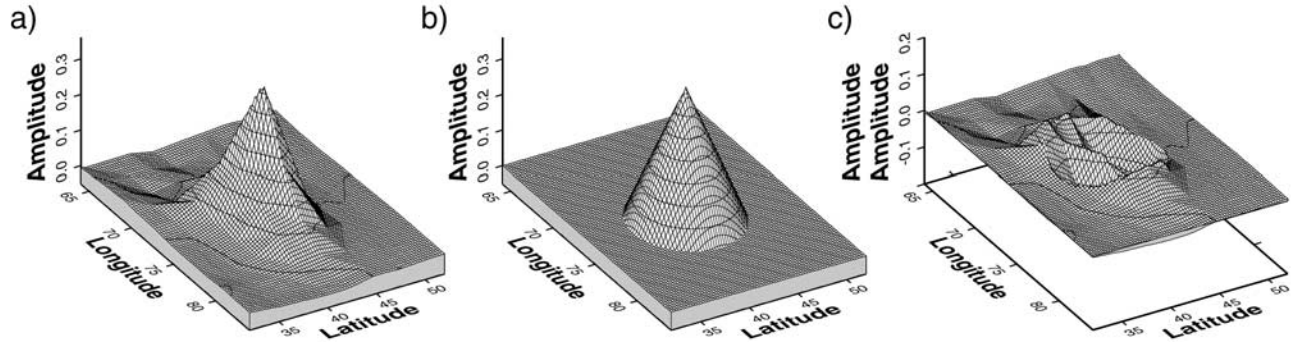

Figure 13. Resolution method. (a) For each grid point on the globe we construct the resolution kernel, which is a row of the resolution matrix and can be presented as a map. (b) We fit a cone to the kernel and identify the resolution with the full width at half maximum height of the cone. (c) Typically, a cone fits well, as shown by the difference between the resolution kernel and best fitting cone. For perfect resolution, the resolution kernel would have a single nonzero point, implying a resolution of $M \times 111$ km on a $M^\circ \times M^\circ$ grid.

The cross correlation between two maps, m and $\tilde{m}$, represented with fully normalized complex spherical harmonics is given by

$$\rho_c(\ell) = \frac{\sum_m c_\ell^{m*} \tilde{c}_\ell^m}{\left[\sum_m |c_\ell^m|^2\right]^{1/2} \left[\sum_m |\tilde{c}_\ell^m|^2\right]^{1/2}}. \quad (11)$$

The associated confidence for each degree correlation coefficient is computed using the formalism of *Eckhardt* [1984]. Power spectral densities, correlation coefficients, and confidence of correlation are presented for Rayleigh wave group velocities at a number of periods in Figures 11 and 12. These results are global averages, and there will be regional variations, of course.

[22] Figure 11 shows that at each period there is a characteristic ℓ band in which the power in the diffraction tomography map is greater than that in the Gaussian tomography. This band shifts to lower ℓ as period increases. Thus the main difference in the amplitudes produced by the two tomographic methods, noted in Figures 8 and 9, derives from a limited ℓ band. At 150 s, for example, this band extends from ℓ of 10 to 30, but at 20 s it extends from about 20 to 55. Irrespective of period, the two methods retrieve nearly identical power at low ℓ. At a large ℓ value that depends on period, each Gaussian tomography power

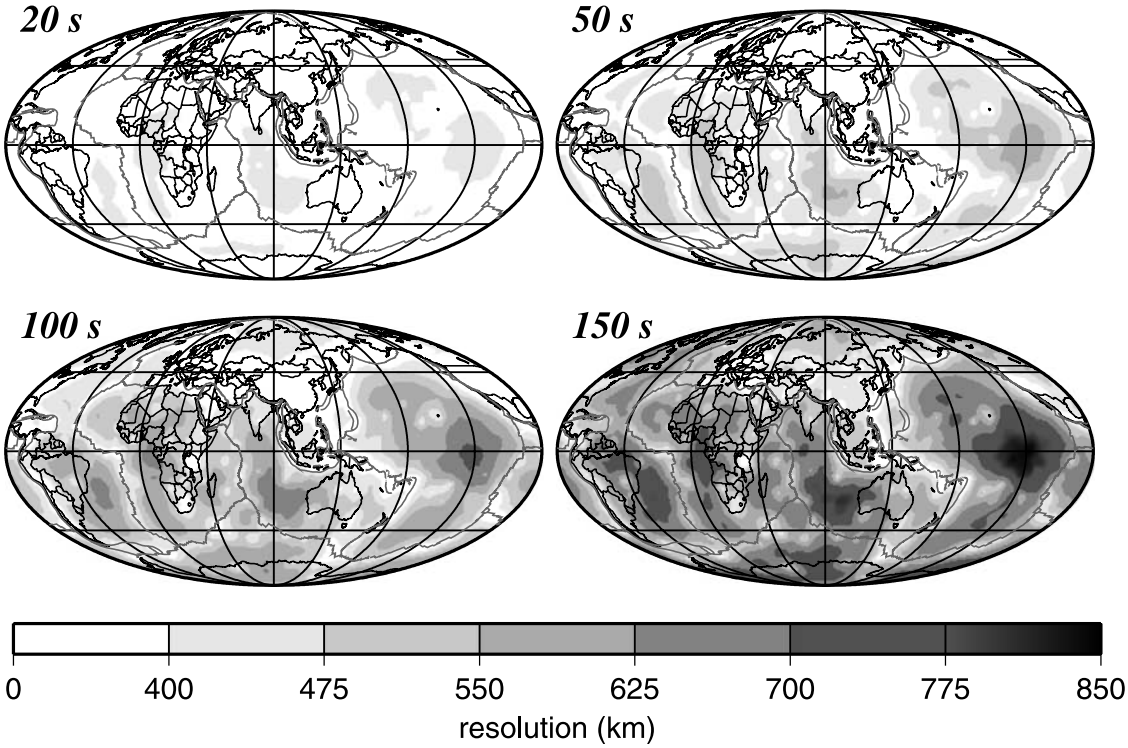

Figure 14. Resolution estimates from diffraction tomography for 20–150 s Rayleigh wave group velocities. Resolution is determined on a $3^\circ \times 3^\circ$ grid, so optimal resolution would be 333 km.

spectrum crosses over the diffraction tomography spectrum. This accounts for the greater smoothness to the edges of the diffraction tomography features noted in Figures 8 and 9. The Gaussian tomography maps are enriched in the shortest wavelength features, and the results of diffraction tomography call these features into question.

[23] A comparison between the geometry of the maps from the two tomographic methods is presented in Figure 12. Not surprisingly, Figure 12a shows that the correlation is best at short periods where the sensitivity zones are, on average, narrowest. Confidence of correlation helps to interpret the raw correlation coefficients, and Figure 12b reveals a period-dependent characteristic cutoff in ℓ above which correlation significantly degrades. Using the 90% confidence level for this cutoff, correlations degrade for the 150 s map above $\ell \approx 18$, at 100 s above $\ell \approx 30$, at 50 s above $\ell \approx 45$, and at 20 s correlation extends at least to $\ell = 60$. This is consistent with the results of *Spetzler et al.* [2001], who present similar bounds for the application of ray theory. It should be remembered, however, that the details of these results depend on the choice of N in equation (1), which remains the subject of debate, as well as other approximations described above.

5. Resolution

[24] A principal problem with tomographic methods that are based on ray theory with ad hoc smoothing constraints, such as Gaussian tomography, is that they yield inaccurate resolution estimates. We show here that there are probably more significant differences between the resolution estimates that derive from Gaussian and diffraction tomography than between the maps themselves. To estimate resolution, we use the method described by *Barmin et al.* [2001]. In this method, each row of the resolution matrix is a resolution kernel on a global map that approximates the response of the tomographic procedure to a δ-like perturbation at a target node. An example is shown in Figure 13a. This information is summarized for each spatial node by fitting a cone to the resolution kernel (Figure 13b). We use a cone because of the bilinear interpolation procedure that defines values of the map between nodal points. A δ function, nonzero at only one node of the grid, in fact is interpreted as a cone whose radius at its base is equal to the grid spacing. Resolution kernels, therefore, tend to be conical in shape. In most cases, the best fit cone fits the resolution map well (Figure 13c). We summarize the large quantity of information in the resolution maps with a single number to indicate the resolution at each node, which we define as the radius at the base of the best fit cone. The resolution cannot be less than M, where M is the distance between the nodes on the tomographic grid. This definition of resolution is half of the value used by *Barmin et al.* [2001] but appears to be more consistent with common usage. In the example in Figure 13, nodes are separated by 2 equatorial degrees ($\sim$222 km).

[25] Figure 14 presents plots of resolution estimates for Rayleigh wave group velocities at a variety of periods. For these results, damping is independent of period. Unlike the tomographic maps shown in Figures 8 and 9, these resolution estimates are constructed on a $3^\circ \times 3^\circ$ grid so that optimal resolution would be $\sim$333 km. Resolution varies greatly over the Earth's surface at each period, locally reflecting the average sensitivity zone width, and is, therefore, substantially worse in oceans than on continents, on average. Resolution also degrades with increasing period as sensitivity zones widen. The worst resolution in our data set is in the central Pacific and the southern Indian and Atlantic Oceans away from ridge crests, where it degrades to values as high as 850 km at long periods. The average resolution over the globe is shown in Figure 15 for both Rayleigh and Love waves. Average resolution from diffraction tomography ranges from a nearly optimal 350 km at 20 s period to about 700 km at 200 s for Rayleigh waves, and from 500 km to about 1200 km from 20 s to 150 s for Love waves. Much of this difference in resolution between Rayleigh and Love waves come from the poor Love wave data coverage across much of the Pacific. Resolution differences between Rayleigh and Love waves on continents are much smaller. In contrast, the resolution from Gaussian tomography is much flatter, both with period and geographically. In previous applications of Gaussian tomography [e.g., *Levshin et al.*, 2001; *Ritzwoller et al.*, 2001], we increased the Gaussian smoothing width with period to degrade resolution, but these attempts still did not produce resolution estimates as low as those that emerge from diffraction tomography.

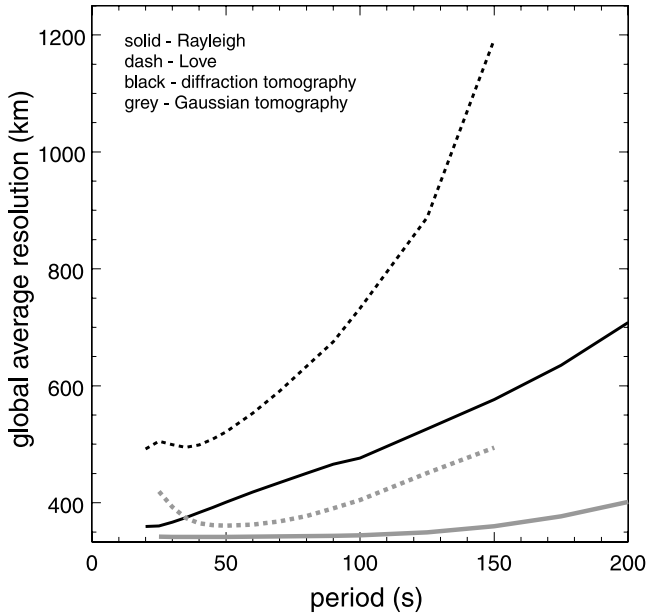

Figure 15. Global average resolution plotted versus period for Rayleigh (solid) and Love (dashed) waves where diffraction tomography results are black and Gaussian tomography results are grey. The Gaussian tomography resolution estimates are unreliable, particularly at long periods. Resolution is determined on a $3^\circ \times 3^\circ$ grid, so optimal resolution would be 333 km.

6. Discussion

[26] There are substantial differences between Gaussian (i.e., ray theoretic) and diffraction tomography as shown by Figures 8 and 9. Our estimates of these differences depend on the definition of the extent of the sensitivity zone (N in equation (1)), about which there is currently debate, as well

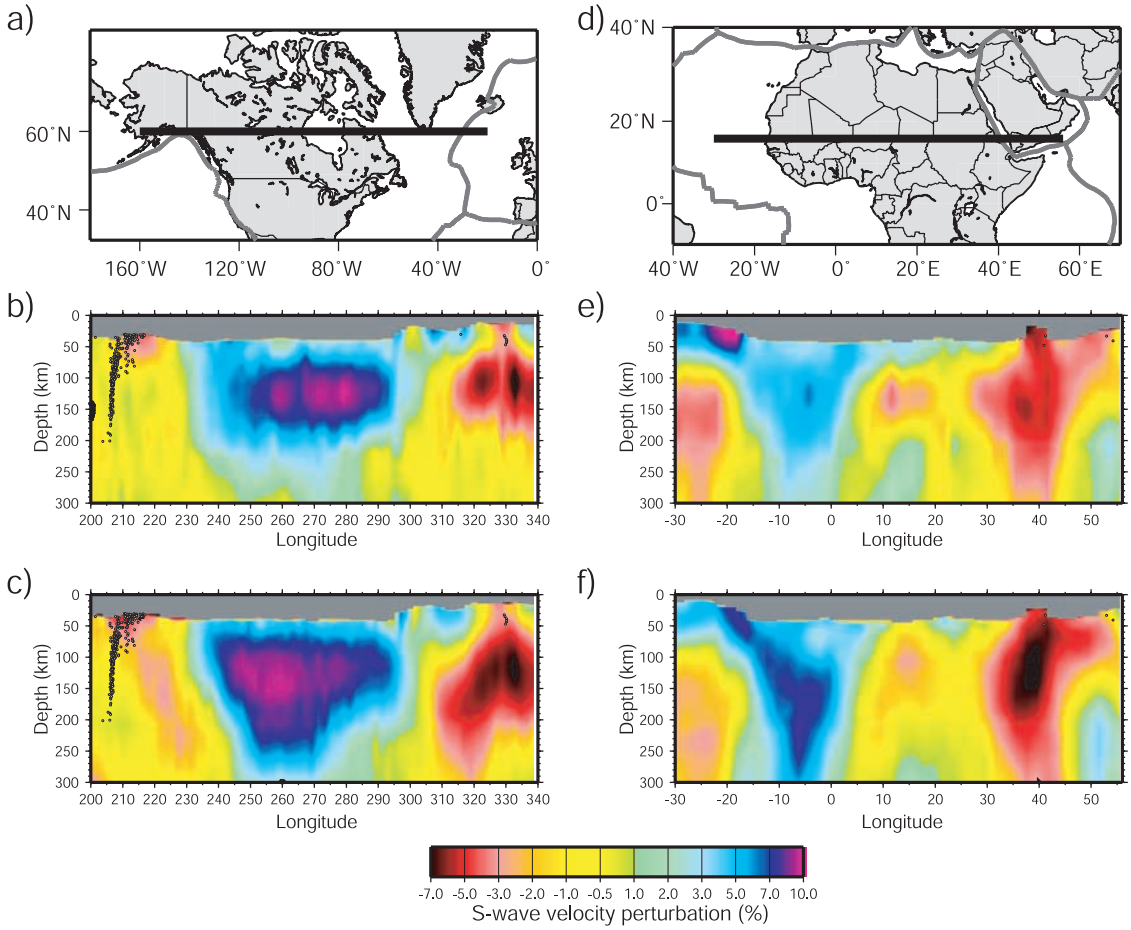

Figure 16. Examples of how diffraction tomography affects the depth extent of mantle features. (a) Location of the vertical slice through the Canadian shield. (b) Slice through the shear velocity model constructed with Gaussian tomography. (c) Slice through the model constructed with diffraction tomography. (d–f) Same as Figures 16a–16c, but for a slice through Africa. Anomalies are presented as percent perturbations relative to the 1-D model ak135 [*Kennett et al.*, 1995]. Earthquake locations are identified.

as the distribution of our current data set. Independent of the choice of N, however, differences between the methods will be greatest at long periods for long paths. This means that, on average, diffraction tomography is most important in oceanic regions, but it is also important on continents at long periods. Diffraction tomography affects both the geometrical pattern and the amplitude of the estimated tomographic features. At each period, the correlation between the Gaussian and diffraction tomographic maps is high up to a critical spherical harmonic degree or structural wavelength. The value of this critical wavelength depends strongly on the choice of N in equation (2). Spherical harmonic power spectra reveal that diffraction tomography retrieves higher amplitude anomalies in a discrete period-dependent ℓ band. This band at long periods extends from about $\ell = 10$ to 35, which is of crucial importance for imaging upper mantle structures relevant to tectonic interpretation.

[27] An example of the effect of these differences between Gaussian and diffraction tomography is found in Figure 16, which shows two vertical slices through two shear velocity models. One model is constructed from the dispersion maps derived from Gaussian tomography and the other from the diffraction tomography maps with the same data sets and damping parameters. The differences between the models are mainly caused by the fact that the amplitudes of the long-period diffraction tomography anomalies are typically larger than analogous anomalies from Gaussian tomography at the principal lengths scales of these models (i.e., $\sim 10 \leq \ell \leq \sim 35$). The result is that mantle features inferred from diffraction tomography tend to have larger amplitudes and extend deeper than those from the Gaussian tomography. Thus, the Canadian and West African cratons extend deeper in Figures16c and 16f than in Figures 16b and 16e, respectively. Low-velocity, asthenospheric anomalies, such as those beneath the North Atlantic Ridge and the Red Sea, also extend deeper into the mantle with diffraction tomography. In general, the depth extent of model features in the upper mantle depends in detail on approximations made in modeling the surface wave sensitivities.

[28] There remain a number of natural directions in which to move to advance methods designed to improve the practical application of surface wave scattering theories. Most importantly, further investigations with numerical experiments are needed to refine the extent of the sensitivity

zone (e.g., the value of N) and the shape of the Fréchet sensitivity kernels, to determine the importance of distinguishing between group and phase velocity kernels, and to investigate the deformation of sensitivity zones caused by heterogeneity particularly at periods below ~30 s. Finally, it remains to be determined how azimuthal anisotropy estimates will be affected by modeling scattering through both isotropic and anisotropic structures.

[29] **Acknowledgments.** We would like to thank Roel Snieder for encouraging our work on this problem, Tatiana Yanovskaya for providing the ray tracing code used to construct Figure 5, and Jeannot Trampert and an anonymous reviewer for helpful referee reports. All maps were generated with the Generic Mapping Tools (GMT) data processing and display package [*Wessel and Smith*, 1991, 1995]. Aspects of this research were supported by grants from the Office of Polar Programs of the U.S. National Science Foundation, NSF-OPP-9615139 and NSF-OPP-9818498, and by contracts from the Defense Threat Reduction Agency, DTRA01-99-C-0019 and DTRA01-00-C-0013.

References

Barmin, M. P., A. L. Levshin, and M. H. Ritzwoller, A fast and reliable method for surface wave tomography, *Pure Appl. Geophys.*, *158*, 1351–1375, 2001.

Bostock, M. G., and B. L. N. Kennett, Multiple scattering of surface waves from discrete obstacles, *Geophys. J. Int.*, *108*, 52–70, 1992.

Chevrot, S., J. P. Montagner, and R. Snieder, The spectrum of tomographic Earth models, *Geophys. J. Int.*, *133*, 783–788, 1998.

Dahlen, F. A., Multiplet coupling and the calculation of synthetic long-period seismograms, *Geophys. J. R. Astron. Soc.*, *91*, 241–254, 1987.

Dahlen, F. A., S.-H. Hung, and G. Nolet, Fréchet kernels for finite-frequency traveltimes, I, Theory, *Geophys. J. Int.*, *141*, 157–174, 2000.

Deuss, A., and J. H. Woodhouse, Theoretical free-oscillation spectra: The importance of wide band coupling, *Geophys. J. Int.*, *146*(3), 833–842, 2001.

Dziewonski, A. M., and D. L. Anderson, Preliminary Reference Earth Model, *Phys. Earth Planet. Inter.*, *25*, 297–356, 1981.

Eckhardt, D. H., Correlations between global features of terrestrial fields, *Math. Geol.*, *16*(2), 155–171, 1984.

Edmonds, A. R., *Angular Momentum in Quantum Mechanics*, Princeton Univ. Press, Princeton, N. J., 1960.

Friederich, W., Propagation of seismic shear and surface waves in a laterally heterogeneous mantle by multiple forward scattering, *Geophys. J. Int.*, *136*, 180–204, 1999.

Friederich, W., East Asian mantle structure from shear and surface waveforms, *Eos Trans. AGU*, *82*(47), Fall Meet. Suppl., Abstract S52F-0694, 2001.

Friederich, W., E. Wielandt, and S. Strange, Multiple forward scattering of surface waves: Comparison with an exact solution and the Born single-scattering methods, *Geophys. J. Int.*, *112*, 264–275, 1993.

Katzman, R., L. Zhao, and T. H. Jordan, High-resolution, two-dimensional vertical tomography of the central Pacific using *ScS* reverberations and frequency-dependent travel times, *J. Geophys. Res.*, *103*, 17,933–17,971, 1998.

Kennett, B. L. N., E. R. Engdahl, and R. Buland, Constraints on seismic velocities in the Earth from travel times, *Geophys. J. Int.*, *122*, 108–124, 1995.

Levshin, A. L., M. H. Ritzwoller, M. P. Barmin, and A. Villaseñor, New constraints on the Arctic crust and uppermost mantle: Surface wave group velocities, P_n, and S_n, *Phys. Earth Planet. Inter.*, *123*, 185–204, 2001.

Li, X.-D., and T. Tanimoto, Waveforms of long-period body waves in a slightly aspherical Earth model, *Geophys. J. Int.*, *112*, 92–102, 1993.

Li, X.-D., and B. Romanowicz, Comparison of global waveform inversion with and without considering cross-branch modal coupling, *Geophys. J. Int.*, *121*, 695–709, 1995.

Li, X.-D., and B. Romanowicz, Global mantle shear-velocity model developed using nonlinear asymptotic coupling theory, *J. Geophys. Res.*, *101*, 22,245–22,272, 1996.

Lomax, A., The wavelength-smoothing method for approximating broadband wave propagation through complicated velocity structures, *Geophys. J. Int.*, *117*, 313–334, 1994.

Marquering, H., and R. Snieder, Surface-wave mode coupling for efficient forward modelling and inversion of body-wave phases, *Geophys. J. Int.*, *120*, 186–208, 1995.

Marquering, H., G. Nolet, and F. A. Dahlen, Three-dimensional waveform sensitivity kernels, *Geophys. J. Int.*, *132*, 521–534, 1998.

Marquering, H., F. A. Dahlen, and G. Nolet, Three dimensional sensitivity kernels for finite-frequency travel times: the banana-doughnut paradox, *Geophys. J. Int.*, *137*, 805–815, 1999.

Meier, T., S. Lebedev, G. Nolet, and F. A. Dahlen, Diffraction tomography using multimode surface waves, *J. Geophys. Res.*, *102*, 8255–8267, 1997.

Nolet, G., and F. A. Dahlen, Wave front healing and the evolution of seismic delay times, *J. Geophys. Res.*, *105*, 19,043–19,054, 2000.

Park, J., Asymptotic coupled-mode expressions for multiplet amplitude anomalies and frequency shifts on an aspherical Earth, *Geophys. J. R. Astron. Soc.*, *90*, 129–169, 1987.

Pollitz, F., Scattering of spherical elastic waves from a small-volume spherical inclusion, *Geophys. J. Int.*, *134*, 390–408, 1998.

Ritzwoller, M. H., and A. L. Levshin, Eurasian surface wave tomography: Group velocities, *J. Geophys. Res.*, *103*, 4839–4878, 1998.

Ritzwoller, M. H., N. M. Shapiro, A. L. Levshin, and G. M. Leahy, Crustal and upper mantle structure beneath Antarctica and surrounding oceans, *J. Geophys. Res.*, *106*, 30,645–30,670, 2001.

Romanowicz, B., Multiplet-multiplet coupling due to lateral heterogeneity: Asymptotic effects on the amplitude and frequency of the Earth's normal modes, *Geophys. J. R. Astron. Soc.*, *90*, 75–100, 1987.

Shapiro, N. M., and M. H. Ritzwoller, Monte Carlo inversion for a global shear velocity model of the crust and upper mantle, *Geophys. J. Int.*, *151*, 88–105, 2002.

Snieder, R., Scattering of surface waves, in *Scattering and Inverse Scattering in Pure and Applied Science*, edited by R. Pike and P. Sabatier, pp. 562–577, Academic, San Diego, Calif., 2002.

Snieder, R., and B. Romanowicz, A new formalism for the effect of lateral heterogeneity on normal modes and surface waves, I, Isotropic perturbations, perturbations of interfaces and gravitational perturbations, *Geophys. J. R. Astron. Soc.*, *92*, 207–222, 1988.

Spetzler, J., J. Trampert, and R. Snieder, Are we exceeding the limits of the great circle approximation in global surface wave tomography?, *Geophys. Res. Lett.*, *28*, 2341–2344, 2001.

Spetzler, J., J. Trampert, and R. Snieder, The effect of scattering in surface wave tomography, *Geophys. J. Int.*, *149*, 755–767, 2002.

Vasco, D. W., J. E. Peterson, and E. L. Majer, Beyond ray tomography: Wavepath and Fresnel volumes, *Geophysics*, *60*, 1790–1804, 1995.

Wang, Z., and F. A. Dahlen, Validity of surface-wave ray theory on a laterally heterogeneous Earth, *Geophys. J. Int.*, *123*, 757–773, 1995.

Wessel, P., and W. H. F. Smith, Free software helps map and display data, *Eos Trans. AGU*, *72*, 441, 1991.

Wessel, P., and W. H. F. Smith, New version of the Generic Mapping Tools released, *Eos Trans. AGU*, *76*, 329, 1995.

Wielandt, E., On the validity of the ray approximation for interpreting delay times, in *Seismic Tomography*, edited by G. Nolet, pp. 85–98, D. Reidel, Norwell, Mass., 1987.

Woodhouse, J. H., Surface waves in a laterally varying layered structure, *Geophys. J. R. Astron. Soc.*, *37*, 461–490, 1974.

Woodhouse, J. H., and T. P. Girnius, Surface waves and free oscillations in a regionalized Earth model, *Geophys. J. R. Astron. Soc.*, *68*, 653–673, 1982.

Yanovskaya, T. B., and P. G. Ditmar, Smoothness criteria in surface wave tomography, *Geophys. J. Int.*, *102*, 63–72, 1990.

Yomogida, K., Fresnel-zone inversion for lateral heterogeneities in the Earth, *Pure Appl. Geophys.*, *138*, 391–406, 1992.

Yomogida, K., and K. Aki, Amplitude and phase data inversions for phase velocity anomalies in the Pacific Ocean basin, *Geophys. J. R. Astron. Soc.*, *88*, 161–204, 1987.

Yoshizawa, K., and B. L. N. Kennett, Surface wave tomography: A three-stage approach, *Eos Trans. AGU*, *82*(47), Fall Meet. Suppl., Abstract S52-0698, 2001.

Yoshizawa, K., and B. L. N. Kennett, Determination of the influence zone for surface wave paths, *Geophys. J. Int*, *149*, 441–454, 2002.

Zhao, L., T. H. Jordan, and C. H. Chapman, Three-dimensional Fréchet differential kernels for seismic delay times, *Geophys. J. Int.*, *141*, 558–576, 2000.

Zhao, L., L. Chen, and T.H. Jordan, Full three-dimensional tomography experiments in the western Pacific region, *Eos Trans. AGU*, *82*(47), Fall Meet. Suppl., Abstract S52-0698, 2001.

M. P. Barmin, A. L. Levshin, M. H. Ritzwoller, and N. M. Shapiro, Department of Physics, University of Colorado at Boulder, Boulder, CO 80309-0390, USA. (barmin@ciei.colorado.edu; levshin@ciei.colorado.edu; ritzwoller@ciei.colorado.edu; nshapiro@ciei.colorado.edu)